Geophysical Journal International

Geophys. J. Int. (2024) **237,** 419–435
Advance Access publication 2024 February 2
GJI Geodynamics and Tectonics

https://doi.org/10.1093/gji/ggae044

A tale of two faults: statistical reconstruction of the 1820 Flores Sea earthquake using tsunami observations alone

T. Paskett,[1] J. P. Whitehead,[2] R.A. Harris,[3] C. Ashcraft,[4] J. A. Krometis,[5,6] I. Sorensen[7] and R. Wonnacott[8]

[1]*Rincon Research Corporation, Tucson, AZ* 85711, *USA*
[2]*Mathematics Department, Brigham Young University, Provo, UT* 84602, *USA. E-mail: whitehead@mathematics.byu.edu*
[3]*Geology Department, Brigham Young University, Provo, UT* 84602, *USA*
[4]*United States Geological Survey, Menlo Park, CA* 94025, *USA*
[5]*National Security Institute, Virginia Tech, Blacksburg, VA* 24060, *USA*
[6]*Mathematics Department, Virginia Tech, Blacksburg, VA* 24060, *USA*
[7]*Mechanical Engineering, Brigham Young University, Provo, UT* 84602, *USA*
[8]*Mathematics Department, University of Maryland, College Park, MD* 20742-4015, *USA*

Accepted 2024 February 1. Received 2024 January 19; in original form 2023 September 15

SUMMARY

Using a Bayesian approach we compare anecdotal tsunami runup observations from the 29 December 1820 Flores Sea earthquake with close to 200 000 tsunami simulations to determine the most probable earthquake parameters causing the tsunami. Using a dual hypothesis of the source earthquake either originating from the Flores Thrust or the Walanae/Selayar Fault, we found that neither source perfectly matches the observational data, particularly while satisfying seismic constraints of the region. Instead both posteriors have shifted to the edge of the prior indicating that the actual earthquake may have run along both faults.

Key words: Tsunamis; Historical seismicity; Historical earthquake; Bayesian inversion.

1 INTRODUCTION

A thorough understanding of seismic history in tectonically active regions is necessary to determine the risk of future seismic hazards. The challenge of this need is that faults have seismic events at time scales that stretch back well beyond only a century of instrumental records. It is for this reason that there has been a focused effort to quantify past seismic events even though some observations may be unreliable (Newcomb & McCann 1987; Tanioka & Sataka 1996; Nanayama *et al.* 2003; Grimes 2006; Bryant *et al.* 2007; Bondevik 2008; Sieh *et al.* 2008; Jankaew *et al.* 2008; Monecke *et al.* 2008; Meltzner *et al.* 2010, 2012, 2015; Barkan & Ten Brink 2010; Liu & Harris 2014; Reid 2016; Harris & Major 2016; Fisher & Harris 2016; Griffin *et al.* 2018; Martin *et al.* 2019; Ringer *et al.* 2021). A significant concern with the reconstruction of these historical events is the inherent uncertainty that is unavoidably tied to the nature of the observations themselves. Following the work of (Ringer *et al.* 2021; Krometis *et al.* 2021) we apply a Bayesian framework to the task of quantitatively estimating the size and location of the Flores Sea Earthquake from 1820 that resulted in a devastating tsunami that was witnessed in four places throughout the Flores Sea region (Fig. 1).

As shown in (Ringer *et al.* 2021; Krometis *et al.* 2021) the Bayesian approach provides a statistically justified method to generate thousands of tsunami simulations to determine the most probable source of the observed tsunami. Not only does this methodology provide a phenomenological approach toward sampling the earthquake parameter space, but it also automatically quantifies the uncertainty of those parameters as demonstrated below. In the language of statistical inference, we are able to construct a posterior distribution on the set of earthquake parameters that best yields the observed tsunami characteristics. This posterior distribution provides far more information than simply specifying a single earthquake that best fits the observational data, it is a probability distribution on all potentially valid parameters, thus specifying correlations between the different parameters of the earthquake. In addition, the resultant simulated data provides a quantitative probabilistic assessment of the danger posed by a repeated tsunamigenic event of the same magnitude.

The focus of this paper is on the 1820 December 29 earthquake that shook southwest Sulawesi leading to a devastating tsunami. Historical records (Wichmann 1918, 1922) document that the tsunami destroyed much of the settlement near Bulukumba on the SW arm of Sulawesi, and severely damaged the port city of Bima, Sumbawa over 300 km away, as well as causing some tidal disturbance as far away as Sumenep on Madura Island off the NE coast of Java (Fig. 1). For observations of this event, we rely on translations of the Wichmann catalogue (Wichmann 1918, 1922; Harris & Major 2016), which detail earthquakes and tsunamis of the Indonesian archipelago for parts of the 17th, 18th and 19th centuries. This particular event is of significant interest seismically as there are

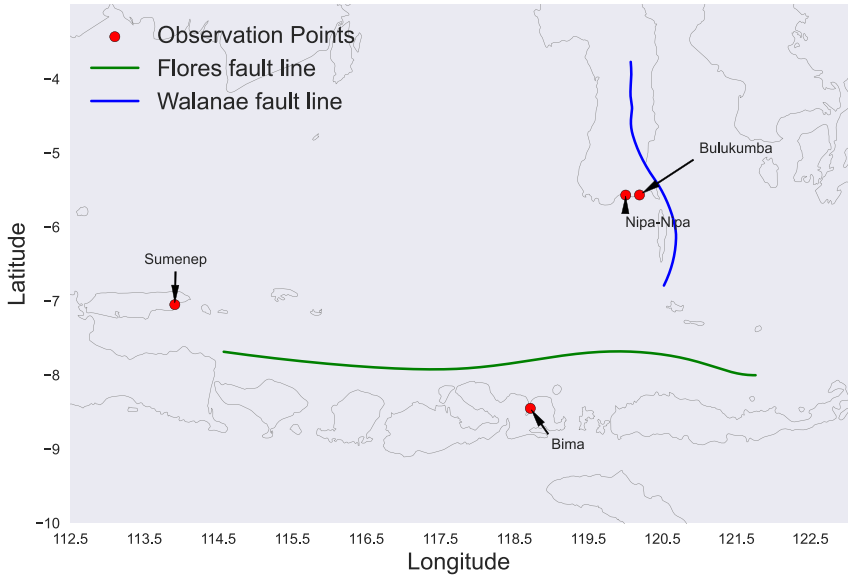

Figure 1. A depiction of the latitude longitude placement of the Walanae/Selayar Fault (blue, striking N–S) and Flores Thrust (gtriking E–W). The red dots are the locations of tsunami observations with Sumenep to the far west, Belukumba and Nip-Nipa to the NE on the SW arm of Sulawesi and Bima in Sumbawa (south of the Flores thrust).

two potential sources of the earthquake: the Flores back-arc thrust (a hypothesis that is investigated in (Griffin *et al.* 2018) for shaking observations of this event), and the more recently quiescent Walanae/Selayar Fault that parallels Selayar Island. The impacts of such a major earthquake at either location on modern society would be devastating. However, it is critically important to determine which of these faults was the source of the 1820 event in order to gauge the potential for future seismic hazards, particularly since there is evidence of Quaternary deformation of the Selayar Island region, but no significant instrumental earthquakes. After constructing two posterior distributions, one for each potential fault source, we note that neither fault 'fits' the historical record, and propose a future approach that will investigate the possibility of a simultaneous rupture of both faults.

2 DATA

There are two types of data relevant to this study which we will discuss in detail below. (i) The historical record of the tsunami event in question as reported in the Wichmann catalogue Wichmann (1918, 1922); Harris & Major (2016) and (ii) modern seismic information of the two faults we consider as potential sources for the event in question.

2.1 Historical observations

2.1.1 The available data

There are four distinct geographical locations with reasonable observations of the tsunami that we make use of as detailed in Table 1. We primarily rely on the translated version of these records given in (Harris & Major 2016), and reproduced below for each observation location. We also note that we are focused on observations of the tsunami, and only make use of the earthquake/shaking observations insofar as they give a relative time from the rupture to the arrival of the first wave.

We have chosen to focus on observations of the tsunami alone, as shaking intensity is notoriously a highly uncertain prediction (Abrahamson *et al.* 2016) particularly without extensive knowledge of VS30 at each observation site. Precise measurements and careful study of the entire Flores Sea region may yield a set of Ground Motion Prediction Equations (GMPE) that fits the ground motion, but to date no such data is available (see Griffin *et al.* 2018) where such a study is carried out with a generic GMPE). As we have a physics-based and rigorously validated (Berger *et al.* 2011) forward model for tsunami propagation, we are more confident in inferring earthquake parameters from observations of the tsunami. Although we do not make direct use of the shaking observations, the historical record of shaking intensity can be used to validate our results as discussed in Section 6.

The relevant portions of the historical record taken from the Wichmann catalogue are listed below for each of these four locations (see Fig. 1 for a depiction of the geographic location of each observation):

Bulukumba:

> ...there was after a weak shock, vibrations becoming gradually more powerful, such that the flat of the commandant in Fort Bulekomba fluctuated to and fro. The six-pounders set up in bastion number 2 hopped from their mounting. After the 4–5 min long quake, shots were believed to be heard in the west, coming from the sea. Barely had the sent envoy returned with the news that ships were nowhere to be seen, than did the sea, under a both whistling and thunder-like rumble, come in, formed as a 60–80 foot high wall, and flooded everything.

Bima:

> Bima on Sumbawa. Violent quake of a good 2 min in duration, which was followed by a violent rumbling and then a flood wave that flung anchored ships far inland and over roof tops.

Nipa-Nipa:

> ...as a result of the flood wave that penetrated 400–500 feet inland, the villages Nipa-Nipa and Terang-Terang. 400–500 persons drown,

Table 1. The historical observations used in this study. Each observation is included if there is reasonable information that details the arrival time of the wave following the earthquake and/or a quantitative measure of the maximal wave height is available.

Location	Type of observation	Original reference
Bulukumba	Arrival time and wave height	(Van Eysinga 1831)
Bima	Wave height	(Anonymous 1852; Reinwardt 1858)
Nipa-Nipa	Wave height	(Van Eysinga 1831)
Sumenep	Arrival time and wave height	(Anonymous 1821)

among whom were 3 Europeans. Multiple vehicles located on the beach were flung onto the rice fields.

Sumenep:

10 a.m. Sumenep [Sumanap], east side of the Island of Madura. Violent, one minute long earthquake that was followed at 3 p.m. by a flood wave.

The quoted phrases given above are taken directly from the English translation of the Wichmann catalogue, which as is pointed out in several locations (see Martin *et al.* 2022) is not the original source material, but a compilation from anecdotal first-person journals and/or newspapers. Although we have relied on the English translation provided by (Harris & Major 2016), we have reviewed the original sources for each of these accounts as indicated in Table 1. Further quotations from original source material are included in the Supplemental material including additional sources beyond those mentioned in Table 1.

2.2 Modern data on seismic sources

We also take advantage of modern observations of the seismic structure of the Flores thrust and Walanae/Selayar fault as well as globally observed relationships for rupture zones. This data is far more reliable and quantitative than the historical record described above, but in the case of the Walanae/Selayar fault, is still quite sparse.

2.2.1 Global data on magnitude of earthquake rupture

The length, width and slip are used to compute the magnitude of a rupture zone, and are highly correlated, that is the aspect ratio of an earthquake rupture zone fits a reasonable log-linear relationship (log base 10; Wells & Coppersmith 1994; Blaser *et al.* 2010) with a substantial amount of deviation, see Fig. 2. Using data from (Wells & Coppersmith 1994) coupled with modern earthquake measurements of megathrust events (see Blaser *et al.* 2010, for example), we constructed a linear regression fit that relates the logarithm (base 10) of the length and width to the magnitude. This fit is depicted in Fig. 2.

2.2.2 Data for the Walanae/Selayar fault

Earthquakes are recorded for most of the Walanae/Selayar Fault (17 events >3.0 M_w) including three quakes of M_w 5.0–5.9 since 1993 (Jaya *et al.* 2020). The section of the fault south of Bulukumba (Belokumba), known as the Selayar Fault, which causes uplift of Selayer Island, is underslipped with 5–10 mm a^{-1} of convergence to the ENE. This fault, which causes uplift of Quaternary coral terraces on Selayar Island, currently may be in a phase of interseismic elastic strain accumulation, but is capable of generating a tsunami (Simons *et al.* 2007; Cipta *et al.* 2017; Sarsito *et al.* 2019).

2.2.3 Data for the Flores thrust

The Flores Thrust forms in the backarc region of the eastern Sunda and Banda volcanic arcs due to distribution of strain away from the Banda arc-continent collision (Silver *et al.* 1983; Hamilton 1979; Harris 2011). The fault strikes E–W and dips around 30° to the south moving the volcanic arc northward over the Flores Sea ocean basin. This motion is driven by the high frictional resistance to subduction of the Australian continent beneath the volcanic arc. The amount of convergence between the Australian and Asian plates that is partitioned to the Flores thrust increases eastward from 21 to 58 per cent (Nugroho *et al.* 2009). Convergence rates along the Flores thrust and its western extension into Java relative to SE Asia increase eastward from 3.4 to 44.0 mm yr^{-1}. in Java and Flores, respectively (Nugroho *et al.* 2009). The increase in rates is due to the distribution of strain away from the thrust front into the back arc region from increasing amounts of arc-continent collision eastward. The two largest recorded earthquakes on the fault were in 1992 (Mw 7.8) and 2004 (Mw 7.5). Both of these earthquakes generated tsunamis, but neither impacted the areas inundated by the 1820 event. The USGS earthquake catalogue lists over one hundred other recorded earthquakes along the Flores thrust, however a large number of these do not have full fault-plane solutions, or are missing some component of the needed fault geometry parameters. We are interested in seismic events large enough to generate a tsunami and do not want to include smaller-scale events that may not have been on the main fault, and hence restrict the data to earthquakes exceeding 5.0 M_w. All remaining events had the following parameters defined in the catalogue: latitude–longitude of the hypocentre, depth, dip and strike. We were left with 94 seismic events in the instrumental record. These fault plane solutions formed the basis for our prior distribution on Flores thrust fault geometry.

3 METHODS

3.1 Bayesian inversion and Markov chain Monte Carlo

For the purposes of the current discussion, we briefly recall the basis for Bayes' Theorem and the use of Markov chain Monte Carlo (MCMC) in identifying the earthquake parameters most likely associated with the 1820 event. Rather than reviewing all of the details, we will provide a succinct summary and focus on those aspects of the inverse problem particular to this event. A more detailed description of the approach taken here is provided in (Krometis *et al.* 2021), and more generally in Kaipio & Somersalo (2005) and Gelman *et al.* (2014). We do, however, focus on the application of Bayes' Theorem to the problem at hand, determining a reasonable probability distribution on parameters meant to model an earthquake given statistical observations of the resultant tsunami wave height and arrival time at different locations.

Our goal in this study is to determine the most probable earthquake that best matches the data described previously. If we refer to

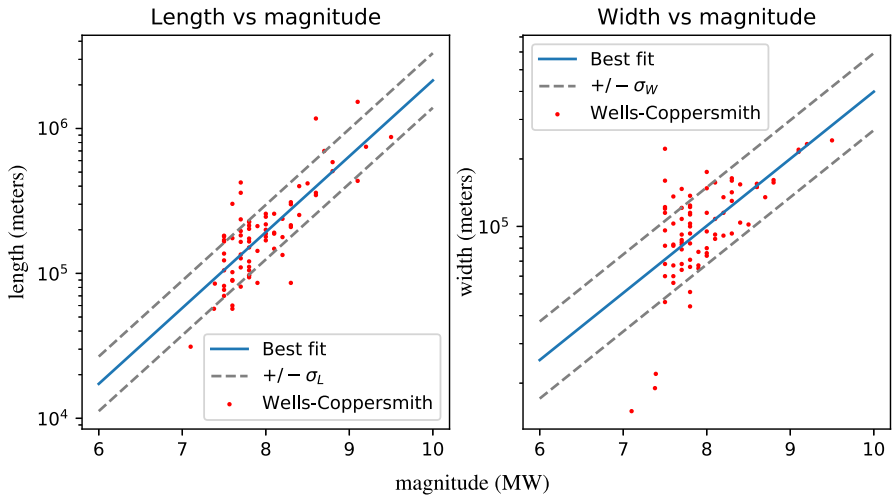

Figure 2. Wells–Coppersmith and modern data plotted alongside linear best fits for $\log l$ and $\log w$ against magnitude M. This is fig. 3 from Ringer *et al.* (2021).

$\tilde{x}$ as the earthquake parameters, then we seek to identify, or at least approximate the conditional probability distribution $\pi(\tilde{x}|\mathcal{O})$, where $\mathcal{O}$ are the historical observations that we have obtained from the historical accounts. In other words we are going to approximate the probability of a specific set of Okada earthquake parameters (Okada 1985, 1992), given the observations from the historical record.

The natural way to compute $\pi(\tilde{x}|\mathcal{O})$ is to apply Bayes' Theorem which states that this *posterior* probability is proportional to the product of a *prior* $\pi(\tilde{x})$ and *likelihood* $L(\mathcal{O}|\tilde{x})$, that is

$$\pi(\tilde{x}|\mathcal{O}) = \frac{\pi(\tilde{x})L(\mathcal{O}|\tilde{x})}{\pi(\mathcal{O})}, \tag{1}$$

where the denominator $\pi(\mathcal{O})$ is the probability of the observations occurring (essentially an impossible distribution to compute exactly). The prior $\pi(\tilde{x})$ is a distribution that represents the *a priori* expert knowledge of the potential distribution of earthquake parameters before examining the observational data, and $L(\mathcal{O}|\tilde{x})$ represents the likelihood of the historical observations occurring given a specific set of earthquake parameters $\tilde{x}$. Specifying the prior and likelihood will then describe the desired posterior distribution up to the constant value given by the denominator.

The description above explains the computation of the relative posterior probability for a particular set of parameters. Approximating the full posterior distribution (i.e. identifying the denominator from the above) is a much more difficult task. To adequately approximate the full distribution we use MCMC (Kaipio & Somersalo 2005; Gelman *et al.* 2014) which generates a Markov chain whose stationary distribution converges to the desired posterior. For the computations performed here, we have utilized a random walk proposal kernel that takes randomized steps in parameter space between each proposed earthquake. For example, suppose that we are currently considering earthquake parameters $\tilde{x}_k$, and have computed the prior probability $\pi(\tilde{x}_k)$, and after passing these parameters through our forward model (discussed below), also computed the likelihood $L(\mathcal{O}|\tilde{x}_k)$. The next step is to select a new set of earthquake parameters $\tilde{y} = \tilde{x}_k + \eta$ (referred to as the proposal), where η is a random variable with a prescribed covariance matrix (chosen to yield the optimal mixing and convergence of the Markov Chain). The prior and likelihood of $\tilde{y}$ are computed. The proposal $\tilde{y}$ is then *accepted* based on the relative probability:

$$\alpha = \min\left(\frac{\pi(\tilde{y})L(\mathcal{O}|\tilde{y})}{\pi(\tilde{x}_k)L(\mathcal{O}|\tilde{x}_k)}, 1\right), \tag{2}$$

that is we accept the proposal if it has a relatively higher probability than the current sample $\tilde{x}_k$, but may also accept the proposal (with lower probability) even if the posterior probability is less. If the proposal is accepted then $\tilde{x}_{k+1} = \tilde{y}$ and otherwise $\tilde{x}_{k+1} = \tilde{x}_k$.

We note that due to the underlying structure of the two faults in question here, we are unable to have a single prior distribution $\pi(x)$ on the earthquake parameters. Instead we specify two separate prior distributions, one for the Flores thrust and one for the Walanae/Selayar fault which then correspond to two distinct posterior distributions, that is we repeat the MCMC steps outlined above for both scenarios and construct both approximate posterior distributions.

Tuning the proposal kernel of MCMC may help accelerate convergence, but it is still possible that, after a finite (even large) number of samples have been collected, the chains have failed to converge. A standard metric for convergence when multiple chains can be compared is the *Gelman–Rubin diagnostic R* (Gelman *et al.* 1992). R is a measurement of the extent to which the chains have converged to the same distribution. When R is close to 1, and generally less than 1.1 or 1.2, the chains are all mixing around the same distribution, presumably the posterior. We make use of this diagnostic below to verify that our MCMC chains are truly converging. Another informal diagnostic used in practice is the average acceptance rate, that is the number of accepted samples. For random walk MCMC, the formally ideal acceptance rate is 23.4 per cent (Gelman *et al.* 1997), so chosen to tune the sampler, not necessarily to define convergence of the posterior.

3.2 Construction of the prior distributions: model parameters and sample parameters

Although the components of the earthquake model are all clearly dependent on one another, that dependence is functionally difficult to assign (explicitly determining how the dip and magnitude are related for instance is not an easy task) and so we assume that most aspects of the prior distribution are independent from one another meaning that we can construct the prior as multiplicative parts,

that is

$$\pi(\tilde{x}) = \pi_0(\tilde{x_0})\pi_1(\tilde{x_1}),$$

where $\tilde{x} = (\tilde{x_0}, \tilde{x_1})$ makes up the sample space and π_0 and π_1 are two independent probability distributions.

3.2.1 *The model parameters for an earthquake rupture*

To determine the posterior distribution we first need to create a prior distribution on the earthquake parameters, that is we need to determine what $\pi(\tilde{x})$ is for our setting. As mentioned previously, for earthquake induced tsunamis, we will consider earthquakes parametrized by the Okada model (Okada 1985, 1992) which is dictated by a set of nine model parameters in three distinct categories of magnitude, location and orientation/geometry.

The magnitude of the rectangular earthquake (our choice of model for this study) is fully described by the length, width and slip of the rupture. The length l is the horizontal length of a rectangular rupture zone (typically measured in kilometres). The width w is the width of the same rectangular rupture zone (typically measured in kilometres). The slip s is the amount of movement the rectangular rupture zone sustained during the seismic event (typically measured in meters). Our model will assume a uniform slip distribution throughout the entire rectangular region. The scalar seismic moment M_0 of the earthquake is calculated from these three parameters via

$$M_0 = \mu l w s, \tag{3}$$

where $\mu = 4 \times 10^{10}$ Pa is the shear modulus (rigidity constant), assumed to be constant for the region in question, and in this case the length l and width w are measured in meters for dimensional consistency. The moment magnitude M_{w} is then defined as

$$M_{\mathrm{w}} = \frac{2}{3}(\log_{10} M_0 - 9.05). \tag{4}$$

We will specifically use the rectangular Okada model so that all ruptures are assumed to be adequately described by a series of connecting rectangles.

We assume that the fault ruptures instantaneously and that the slip is uniformly distributed across the entire length of the rupture. Further parametrization of a time-dependent, non-uniform (in space) rupture is possible with the Okada model but we do not anticipate that our data is sufficiently robust to infer details for such a model, although this will very likely modify our final conclusions. In particular, a uniform slip distribution has been shown to reduce the size of the resultant tsunami, indicating that the posterior distribution of slip that we identify here is likely an overestimate on the actual slip (and hence magnitude, see Geist 2002; Butler *et al.* 2017; An *et al.* 2018; Lay 2018; Davies 2019; Melgar *et al.* 2019; Davies & Griffin 2020) of the causal earthquake.

The location is specified by the latitude, longitude and depth of the earthquake centroid. The latitude *lat* and longitude *lon* provide the horizontal coordinates of the earthquake centroid and the depth d is the depth below the surface of the earth of the centroid (typically measured in kilometres).

The orientation/geometry is specified by the strike, dip and rake of the earthquake. The strike α is the orientation of the fault measured clockwise in degrees from north so that if you stand next to the fault facing the along-strike direction, the fault is dipping to the right. The dip β is the angle of inclination of the fault from horizontal. The rake γ is the slip angle in degrees that the upper block of a fault (hanging wall) moves relative to the strike angle, that is a rake of 90° corresponds to hanging wall slip up the fault parallel to the dip direction, which is a thrust fault.

All of these nine parameters constitute what we refer to as the *model parameters* of the causal earthquake $\tilde{x} = (l, w, s, lat, lon, d, \alpha, \beta, \gamma)^T$. As noted in (Ringer *et al.* 2021; Krometis *et al.* 2021), the standard Okada model parameters $\tilde{x}$ are correlated with each other, and hence it is computationally inefficient to search over each of these parameters separately. Moreover, creating a prior distribution on $\tilde{x}$ as defined above is inefficient as it is difficult to characterize physically realistic earthquakes. Instead, we note that the geometry and depth of the fault explicitly depend on the latitude/longitude location of the epicentre, and the 3 magnitude parameters are highly correlated with respect to the magnitude itself. We address these issues by introducing *sample* parameters x that we search over, from which the *model* parameters $\tilde{x}$ can be computed, that is $\tilde{x} = f(x)$ for some map f. Hence we will first define the *sample* parameters x, the map $f(x)$ and then define a prior distribution $\pi(x)$ over the *sample* parameters x.

3.2.2 *Sample parameters for an earthquake rupture*

There are two fundamental assumptions that we use when deriving the sample parameters from the model parameters. First, we note from Fig. 2 that the magnitude of the earthquake is highly correlated with the length and width of the rupture zone. Even so, we do not want to rely on a regressive fit to the data presented in Fig. 2 as that would overly simplify the relationship. To account for uncertainty (as displayed in Fig. 2 the linear fit is certainly not perfect) in this regression we introduce offset parameters $\Delta\log l$ and $\Delta\log w$ which are deviations from the log-linear relationship between magnitude, length, and width, that is

$$\log l = aM + b + \Delta\log l \tag{5}$$

$$\log w = cM + d + \Delta\log w \tag{6}$$

where a, b, c, d are the coefficients of the linear best fits as shown in Fig. 2. The log-linear relationship is then used to infer a rough relationship between the magnitude and length-width, and these offset sample parameters are used to identify variations from this regressive fit.

Second, the depth, strike, rake and dip can be well approximated as functions of the latitude and longitude given previous fault plane solutions for more recent earthquakes along each of the two faults in question (relying on the modern seismic data as described in the Data section above). To account for geographic variations in the faults and uncertainty in the measurements, we also introduce the offset sample parameters: depth_offset Δd, strike_offset $\Delta\alpha$, dip_offset $\Delta\beta$ and rake_offset $\Delta\gamma$ which represent adjustments to the modelled geometry of the fault.

Hence the *sample* parameters of the earthquake rupture are

$$x = (\Delta\log l, \Delta\log w, M, lat, lon, \Delta d, \Delta\alpha, \Delta\beta, \Delta\gamma),$$

and these are mapped to the model parameters either through (5) and (6), or through the data-informed model of the fault as described next for each fault separately. The prior distribution for $\Delta\log l$, $\Delta\log w$ and M is the same for both faults, and can be specified as three independent distributions as prescribed in Table 2. Hence the prior can be decomposed as

$$\pi(x) = \pi_{\Delta\log l}(\Delta\log l)\pi_{\Delta\log w}(\Delta\log w)\pi_M(M)\pi_{\mathrm{fault}}(lat, lon, \Delta d, \Delta\alpha, \Delta\beta, \Delta\gamma), \tag{7}$$

Table 2. The explicit description of the prior distributions for the components of the prior distribution universal between both faults. The values of σ for the two $\Delta\log$ parameters are exactly the residual values from the log-linear regression depicted in Fig. 2. σ refers to the standard deviation for each probability distribution.

Variable	Prior distribution
$\Delta\log l$	Gaussian ($\mu = 0, \sigma = 0.188$)
$\Delta\log w$	Gaussian ($\mu = 0, \sigma = 0.172$)
M	Exponential ($\lambda = 0.5$) truncated at 9.0
(lat, lon)	pre-image of Gaussian on depth ($\mu = 30$ km, $\sigma = 5$ km, truncated to [2.5, 50]

where π_{fault} is specified either for the Flores or Walanae/Selayar fault as outlined below.

To develop the prior distribution for each fault we create a simplified model based on existing fault-plane solutions. This leads to two very different prior distributions as there is a substantial amount of data to constrain the Flores Thrust, but very little to constrain the geometry and location of the Walanae/Selayar Fault. The full prior for each of these separate faults is then broken down as

$$\pi_{\text{fault}}(lat, lon, \Delta d, \Delta\alpha, \Delta\beta, \Delta\gamma) = \pi_{loc}(lat, lon)\pi_d(\Delta d)\pi_\alpha(\Delta\alpha)\pi_\beta(\Delta\beta)\pi_\gamma(\Delta\gamma), \tag{8}$$

where each fault has unique distributions for each term above (as outlined immediately below). The assumption underlying eq. (8) is that while the latitude–longitude centroid coordinates are dependent on each other, all other sample parameters are independent.

The prior distribution on the latitude–longitude location of the earthquake centroid relies on our informed data (and hence model) of each fault so it is unique to each fault, however the basic setup is universal to both. Rather than implement this prior independent of all other parameters, we follow (Ringer *et al.* 2021) and develop a prior distribution on the latitude–longitude of the centroid by first enforcing a prior distribution on the modelled depth of the rupture zone. A model that predicts the earthquake depth given latitude–longitude for each fault is described below, and will yield a depth for each latitude–longitude coordinate which we then assign a probability based on the depth prior distribution. Hence the prior on latitude–longitude is the pre-image of the depth prior through the expected value of the modelled fault for depth as specified in Table 2. We note that this means that all latitude–longitude centroids that are mapped to the same depth will have the same prior probability.

3.2.3 *Modelling the Flores thrust*

Relative to the relevant features of the fault itself, the available data is sparse and irregular, and despite the recent significant advancements in seismography, there is still a large amount of uncertainty in these measurements (Rawlinson *et al.* 2014). Due to the noisy and inherently irregular nature of this collected earthquake source data, we first created a multidimensional spatial Gaussian process (Williams & Rasmussen 2006) to represent/model the Flores thrust. A Gaussian process is a stochastic process that is specified completely by a mean and covariance function which in our case are functions of the latitude and longitude of the earthquake centroid. At a specific earthquake centroid location, all of the relevant variables of the Gaussian process model follow a Gaussian distribution. We could have utilized a regressive fit to the data, retaining the residual as the stochastic sample parameter (as for the length and width discussed earlier), however the geometric seismic data for the Flores fault is far more sparse and irregular than the data depicted in Fig. 2 which is precisely the setting where Gaussian processes are most viable (Williams & Rasmussen 2006).

To demonstrate how a Gaussian process is formed, suppose that the depth is a function of latitude and longitude, that is $d = F(\xi)$, where $\xi = (lat, lon)$ and we do not have the exact formula for the function F. Suppose that $\hat{d} = (d_1, d_2, \ldots d_N)$ is a vector of all of the estimated depth values from recent seismographic readings. We anticipate that there is some noise in the measurements of the earthquake depth, so we presume that

$$\hat{d} = F(\xi_1, \xi_2, \ldots \xi_N) + \epsilon,$$

where ϵ is a vector of independent identically distributed Gaussian variables (with mean 0 and variance σ^2, a hyperparameter that is selected to model the prior (believed) uncertainty in the measurements).

For the Flores thrust, we first select a Gaussian process prior with mean $\mu(\xi)$ equal to the average depth of the training depths $\hat{d}$. We then define a covariance for the Gaussian process prior as

$$\kappa(\xi, \xi') = \exp\left(\frac{1}{2\sigma^2}\|\xi - \xi'\|_2^2\right), \tag{9}$$

that is the squared exponential distance between the latitude–longitude coordinates ξ and ξ'. If we want to estimate the depths $\bar{d}$ at K different latitude–longitude coordinates ξ_k then according to the Gaussian process prior, both the known points (measured values) and unknown values follow a joint Gaussian distribution:

$$\begin{pmatrix}\hat{d}\\ \bar{d}\end{pmatrix} \sim \mathcal{N}\left(\begin{pmatrix}\mu(\hat{\xi})\\ \mu(\bar{\xi})\end{pmatrix}, \begin{pmatrix}\kappa(\hat{\xi}, \hat{\xi}) + \sigma^2 I & \kappa(\hat{\xi}, \bar{\xi})\\ \kappa(\bar{\xi}, \hat{\xi}) & \kappa(\bar{\xi}, \bar{\xi})\end{pmatrix}\right), \tag{10}$$

where the LHS and the mean are 1-D arrays defined by concatenating the two vectors $\hat{d}$ and $\bar{d}$, while the entries of the covariance above are actually submatrices.

Conditioning on the observed data [the seismologically measured depths $(\hat{\xi}, \hat{d})$] then the predicted depths for locations $\bar{\xi}$ will satisfy (see Williams & Rasmussen 2006, section A.2)

$$\bar{d}|\bar{\xi}, \hat{d}, \hat{\xi} \sim \mathcal{N}(m, K), \tag{11}$$

where

$$m = \kappa(\bar{\xi}, \hat{\xi})\left[\kappa(\hat{\xi}, \hat{\xi}) + \sigma^2 I\right]^{-1} + \mu(\bar{\xi}), \tag{12}$$

$$K = \kappa(\bar{\xi}, \bar{\xi}) - \kappa(\bar{\xi}, \hat{\xi})\left[\kappa(\hat{\xi}, \hat{\xi}) + \sigma^2 I\right]^{-1}\kappa(\hat{\xi}, \bar{\xi}) \tag{13}$$

defines the resultant Gaussian distribution. Hence to predict the depths for a set of latitude–longitude coordinates we consider the mean m given above, and the variance K gives a measure of the uncertainty of that prediction.

This model is used to represent spatial variations in the depth/dip/strike/rake on the Flores fault, as well as the associated random offsets that reflect the variability of these earthquake parameters. This was done by considering the depth, dip, rake, and strike as independent functions of the centroid latitude and longitude of each instrumentally recorded event, and developing a statistical Gaussian process fit using a radial basis function (rbf) kernel with variance $\sigma^2 = 0.75$ (the same σ^2 hyperparameter discussed above) and a normalized noise level in the data itself of 1.0 (see algorithm 3.2 of Williams & Rasmussen 2006, for details). These hyper-parameters are chosen heuristically to maintain a smooth predictive model that also matches the input data well. The independence assumption used here between the different geometric Okada parameters is for ease of implementation, and because while it is clear physically that there is a dependence between the dip and depth for example, it is not immediately obvious how to quantify that dependence.

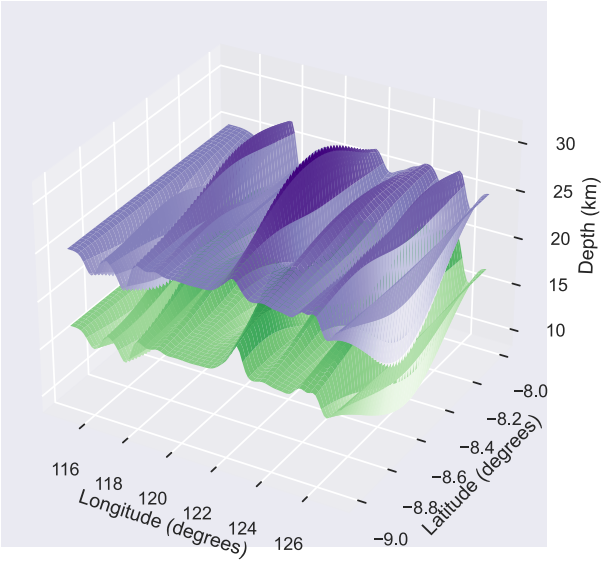

Figure 3. The two surfaces defining one standard deviation away from the mean fit for the depth of the Flores thrust. The Gaussian process for the depth defines the most probable depth as the region between these two surfaces. Note the significant difference in scales between the two axes: this represents a change of only one degree in latitude but 10° in longitude. The difference in scales explains the apparent 'ridged' behaviour of the two surfaces along the longitudinal direction.

Table 3. The standard deviation values for all of the offset parameters for the Flores thrust prior. The model parameters are computed by multiplying the sampled offset parameters (drawn from these prior distributions) by the variance of the Gaussian process at the specific (*lat*, *lon*) value and adding that to the predicted mean of the Gaussian process at that point.

Variable	Standard deviation
d_{off}	$\sigma = 5$ km
α_{off}	$\sigma = 30°$
β_{off}	$\sigma = 5°$
γ_{off}	$\sigma = 45°$

The benefit of using a Gaussian process rather than a standard regression technique is that under the assumed hyperparameters (variance of the kernel, etc.) then the uncertainty is built into the regression. This is demonstrated in Fig. 3 which depicts two depth surfaces that correspond to depths that are one standard deviation away from the mean predicted depth, that is roughly speaking we anticipate that approximately two thirds of the earthquakes on the Flores thrust will be contained between these two surfaces. Similar processes are constructed for the dip, rake and strike of the fault as well.

The mean dip, rake and strike are computed from the Gaussian process model for the sampled latitude–longitude values, and we sample over the novel offset parameters: d_{off}, α_{off}, β_{off}, and γ_{off} which allow for perturbations from the mean statistical model. To compute the final Okada earthquake parameters, we take the computed mean depth, dip, rake and strike and then add the standard deviation of the Gaussian process at that point multiplied by the corresponding offset parameter, that is $\Delta d = K_d(\xi, \xi)d_{\text{off}}$, where ξ is the location of the centroid latitude–longitude for example. The prior distribution for each of these offset parameters is a Gaussian distribution with mean zero, and standard deviation given in Table 3 for each parameter.

Table 4. The standard deviation values for all of the offset parameters for the Walanae/Selayar thrust prior. All of these offset parameters follow a Gaussian process with mean zero. The model parameters are computed by adding these offset values to the mean values predicted by the planar model described in the body of the text. Note that in this case the offset parameters are the same as the Δ parameters, unlike the case for the Flores prior.

Variable	Standard deviation
d_{off}	$\sigma = 5$ km
α_{off}	$\sigma = 3.5°$
β_{off}	$\sigma = 5°$
γ_{off}	$\sigma = 5.5°$

In summary, in addition to the three parameters prescribed for the magnitude of the earthquake we introduce the following sample parameters: latitude, longitude, d_{off}, α_{off}, β_{off} and γ_{off}. These are mapped through the Gaussian process fault model and then the offset parameters are used to produce the Okada earthquake parameters: latitude, longitude, depth, dip, rake and strike.

3.2.4 Modeling the Walanae/Selayar fault

Lack of instrumentally recorded earthquakes on the Selayar fault hinders efforts to properly fit a Gaussian process to model the fault. Limited detail and constraint on the existing data lead us to make a simpler hypothesis for the fault parameters. We modelled the Walanae/Selayar fault as a plane following a default dip of 25°, that is for a given latitude longitude the depth of the fault is calculated assuming that the fault interface dips 25°. The fault strike is measured from different geographic points parallel to the fault and projected perpendicular to the fault line to points interior to the fault itself. Seismic evidence along the Walanae portion of the fault (north of Selayar island) indicate that the fault is most certainly not dip-slip so there is some amount of obliquity, however the actual rake is unknown. Rather than relying on a pure dip-slip assumption, we have proposed some obliquity via a mean rake of $\gamma = 80°$ (as noted below we introduce a rake offset sample parameter that allows for variations from this value).

To account for the uncertainty in this oversimplified model of the Walanae/Selayar fault, we also introduce and search over Δd, $\Delta\alpha$, $\Delta\beta$ and $\Delta\gamma$ (with prior distributions specified in Table 4), thus allowing for some strike-slip motion which is evident on the Walanae section of the fault. In contrast to the Flores thrust, the final Okada parameters are then obtained from simply adding the offset parameters to those computed from the planar model (the offsets in the Flores thrust are first multiplied by the corresponding standard deviation from the Gaussian process fit). This leads to the final set of Okada parameters required by the forward model.

3.3 Construction of the likelihood distribution

There are two primary steps to constructing the likelihood. We first need to interpret the historical record in a quantitative sense to create observational probability distributions, and then we require a forward model that takes the Okada model parameters, generates a tsunami wave and records the arrival times and maximal wave heights at the desired locations. These outputs are then fed into the observational probability distributions to obtain a total likelihood.

3.3.1 *Observational probability distributions*

Here we detail how the anecdotal data is transformed into observational probability distributions. Each historical account of the tsunami is dissected to come up with a quantitative description of the observation. Each of these probability distributions is constructed without referring to the prior information on tectonic knowledge of the region, that is these observations are interpreted independent of any knowledge of the surrounding fault zones.

As already described, the textual accounts illustrate the two types of observations that we make use of for the 1820 tsunami at different geographic locations: the time it takes for the initial wave to reach a specific location (arrival time), and the maximal wave height at a specific location (wave height). Before we proceed, there are a few things worth pointing out about each observation location before we consider the actual observations themselves.

Bulukumba and Nipa-Nipa are both on the southern tip of SW Sulawesi and 20 km apart. The historical record reports that the earthquake lasted 4–5 min that was followed by a tsunami 18–24 m high at Fort Bulukumba that inundated 300–400 m inland destroying villages around Nipa-Nipa and carrying ships off the coast into rice fields. Sumenep is over 700 km WSW of Bulukumba over a relatively shallow sea (much of the Flores Sea is less than 300 m deep) so a wave that reaches both locations would dissipate a significant amount, and take a long time to propagate that far especially through the relatively shallow Flores Sea. Bima, on Sumbawa Island (the southern most observation location), is deep inside a narrow inlet that opens into a bay. It is well known that inlets and bays *can* amplify tsunamis, but capturing such an effect may require simulations at a higher resolution than the available bathymetry allows.

With all of these considerations in mind, we define the observational probability distributions for each observation on a case-by-case basis, some of which are illustrated specifically here. To begin, the reference to wave height being 18–24 m near Bulukumba is more likely to be an overestimate than an underestimate so the observational probability distribution on wave height at Bulukumba is a normal distribution centred at 18 m with a standard deviation of 5 m. Similarly the wave arrival time at Bulukumba is prescribed as a normal distribution centred at 15 min with a standard deviation of 10 min (truncated at a 0 min or instantaneous arrival). This is based on the proximity of Fort Bulukumba to the coast. Admittedly this observational distribution is very loosely constrained by the historical record so reliance on this particular observation isn't warranted.

As there is no time given for the wave arriving at Bima, we make use of the observation of wave height only. Although flinging 'anchored ships far inland' is very graphic, it is not very quantitative. The fact the ships were anchored seems to indicate they were larger than say, just canoes or other small boats. This observation, and the fact that they were flung 'far' inland and over roof tops, indicates a sizeable wave (also see the Supporting Information for more anecdotal accounts for this location). Based on these observations, waves smaller than 1 m are not plausible. So, for Bima's wave height we chose a truncated Gaussian likelihood with mean 10 m, standard deviation 4 m, and a lower bound of 1 m.

The account from Nipa-Nipa has no estimate of wave height but only inundation, which leads to an observational distribution with an assigned mean of 3 m and standard deviation of 2 m. Similarly the tsunami striking Sumenep was observed without any detail so we select a truncated normal distribution centred around 1.5 m with standard deviation of 1 m with a left-hand cut-off of 0.5 m (basically guaranteeing a wave of some sort is noticed at Sumenep).

The final observation is the wave arrival time at Sumenep. In this case the historical record indicates that the wave arrived at Sumenep 5 hr after the earthquake was felt in Bulukumba and Bima. The issue with this particular observation is that the shaking itself was not recorded in Sumenep and so the 5 hr arrival time is inferred from the time recorded in both locations, however Sumenep and Bima/Bulukumba were not on the same 'time zone' (Nguyen *et al.* 2015) and hence the 5 hr arrival time should be considered quite loosely.

From preliminary estimates of the wave speed across the Flores Sea (recall that in open water tsunamis travel very near the linear phase speed $\sqrt{gH}$ where g is the gravitational constant, and H is the water depth), we were unable to legitimately justify a wave originating from any location on either proposed fault and taking even close to 5 hr to reach Sumenep. Hence to construct the observational probability distribution for the arrival time at Sumenep, we went with the hypothesis that Sumenep was in a different local time than the other observation locations which would put the observed time interval at 4 hr rather than 5. With this in mind, we selected a normal distribution with a mean of 240 min (4 hr) and a standard deviation of 45 min.

The final observational probability distributions are illustrated in Fig. 10 as the continuous red curves, and the relevant hyperparameters for each distribution are specified in Table 5.

3.3.2 *The forward model*

We make use of the finite volume based Geoclaw (Berger *et al.* 2011; González *et al.* 2011; LeVeque *et al.* 2011)model that is contained in the distribution of Clawpack 5.6.0 which is the version used in this study. Geoclaw is developed to solve the full non-linear shallow water equations using the Okada model (Okada 1985, 1992) to generate an idealized seafloor deformation which is used for an initial condition. Geoclaw has the capability of rendering both rectangular and triangular faults, but we only take advantage of the former. Unlike the Banda Arc studied in (Ringer *et al.* 2021) both the Flores thrust and Walanae/Selayar Fault are fairly geographically linear and hence are easily modelled by a small number of rectangular faults. In particular we use three (a modelling choice at this level) rectangular faults to model the full rupture zone of each fault.

The Okada rectangular rupture regions are identified via the following process which is a simplification of that employed for the 1852 event in (Ringer *et al.* 2021). The latitude–longitude centroid location is identified via the random walk Monte Carlo step, and the total width and length of the rupture are computed from the sampled magnitude and $\Delta \log l$ and $\Delta \log w$ as described above. The length is split into 3 to allow for a better representation of the curvature of the fault. Splitting the fault further would not be as beneficial because both the Flores and Walanae faults are relatively linear. The rupture is specified as three different rectangular regions, each with the same width. The latitude–longitude centroid of each of these rectangles is identified along a line of equal depth according to the model specified for each fault (the Gaussian process for the Flores thrust etc.) and the orientation is parallel to the modelled fault. The Okada model is used for each of the three subrectangles for a simultaneous, instantaneous rupture.

Following the formation of the seafloor deformation from the 3-rectangular rupture via the Okada model, Geoclaw uses a finite volume formulation (Berger *et al.* 2011) with a dynamically adaptive spatial mesh to simulate the propagation of the resultant tsunami via

Table 5. Observational probability distribution hyper-parameters for all of the anecdotal accounts converted to quantitative distributions.The truncated Normal (Gaussian) distributions are designed to provide a minimal value as indicated.

Observation location and type	Type of distribution	Parameters
Bulukumba wave height	Normal	$\mu = 18$ m, $\sigma = 5$ m
Bulukumba arrival time	Truncated Normal	$\mu = 15$ min, $\sigma = 10$ min (truncate to 0)
Bima wave height	Truncated Normal	$\mu = 10$ m, $\sigma = 4$ m (truncate to 1 m)
Nipa-Nipa wave height	Truncated Normal	$\mu = 3$ m, $\sigma = 2$ m (truncate to 1 m)
Sumenep wave height	Truncated Normal	$\mu = 1.5$ m, $\sigma = 1$ m (truncate to 0.5 m)
Sumenep arrival time	Normal	$\mu = 240$ min, $\sigma = 45$ min

the non-linear shallow water equations. We leave most parameters in Geoclaw as their default values including bottom drag and friction coefficients, and carefully tune the adaptive mesh as described directly below.

The forward propagation of a tsunami wave critically depends on accurately resolving the bathymetry (underwater topography), which is a difficult and pressing issue for all tsunami simulations and studies. For bathymetry we primarily relied on the 1-arcmin etopo data sets available from the open access NOAA database (https://www.ngdc.noaa.gov/mgg/global/global.html), and for the coastline near each observational point we utilize higher resolution Digital Elevation Models (DEM) from the Consortium for Spatial Information (CGIAR-CSI, http://srtm.csi.cgiar.org/srtmdata/). These higher resolution topographical files yield a 3-arcsecond resolution on land, but give no additional information on the subsurface bathymetry. In addition we also took advantage of detailed sounding maps available from the Badan Nasional Penanggulangan Bencana (BNPB or Indonesian National Agency of Disaster Countermeasure, see http://inarisk.bnpb.go.id). To convert these data into digitally accessible information, contours were taken from images exported from the website and then traced and interpolated in arcGIS to produce approximate depths in the same regions as the DEM files. This approach provides a set of bathymetric files that are accurate to around 10–15 arcsec near each observation location with a maximum possible resolution of 3 arcsecond resolution of the bathymetry plays a critical role in the accurate simulation of tsunami propagation, so the uncertainty inherent in our final bathymetry data will have a cascading effect on the inversion process. We anticipate that some of this uncertainty is accounted for in the width of the observational probability distributions, but a full investigation of this bathymetric uncertainty and its effect on the posterior will be pursued in a later study.

We make use of six different levels of refinement, starting with a resolution of 6 arcmin in the open ocean going down to 3 arcsec (to match the bathymetric data) around those parts of the wave that will impact the observation locations directly. The mesh refinement is activated whenever the solution of the linearized backward adjoint equation (Davis & LeVeque 2016) exceeds a specified threshold at the same time that the forward solution does as well. The linearized adjoint solution is computed on a global mesh of 15 arcsec, initialized with an endpoint condition corresponding to pointwise Gaussian sea surface perturbations at each observation location so that the adjoint solution solved backward in time will identify when and where the forward tsunami will be that directly affects each of the observation locations. This dictates where the mesh is refined. The benefit of using the adjoint driven adaptive mesh is that because every one of our Monte Carlo samples uses the same observation locations, then we need only run the linearized adjoint solver one time (hence the global 15 arcsec resolution, while expensive, is a one time cost), and save the corresponding output to be used with the forward runs.

In addition to the dynamically adaptive mesh, we include several statically refined regions at the highest (3 arcsec) resolution. Each of these regions is specified as a series of rectangular subregions that encapsulate each observation location. This is meant to ensure that the incoming wave is accurately captured as it approaches each observation location. For instance, Bima in Sumbawa is located deep inside a bay that must be accurately captured in order to simulate the tsunami reaching Bima (see Fig. 4 for instance), and so we defined several statically refined regions that encapsulate the bay and surrounding coastline as much as possible without unnecessarily refining the grid on land at the same time.

We ran each tsunami simulation for at least 4 hr in physical time (we initially ran the tsunamis for 5 hr, but none of the waves required more than 4 hr to reach Sumenep, so we allowed the samples to run for 4 hr only to save compute time). Running on 24 cores on a single node each of these simulations took approximately 10–12 min of wall-clock time, that is 240–288 core-minutes of compute time.

Wave heights and arrival times were extracted from the Geoclaw output using the previously developed tsunamibayes package (Whitehead 2023). Each of the observations described in Table 5 are then recorded, and observational probabilities are assigned to each. The final likelihood probability is computed as the product of the individual probabilities meaning we assume that all of the observations are independent as there is no foreseen approach that would capture the actual dependence of these observations.

4 RESULTS

4.1 Statistical summary

For each fault we initialized ten different chains with five unique latitude–longitude locations geographically spread across the entire fault and with two different magnitudes, 8.0 and 8.5, for a total of ten initial earthquakes (for each fault). After running each chain for two thousand samples a piece, we resampled all ten chains according to their final posterior probability and restarted each chain accordingly. In this process most of the chains were eliminated, as most had still not achieved a finite log likelihood (most of the chains were unable to generate a noticeable tsunami wave that reached Sumenep). After resampling, each chain was run for a minimum of 9000 samples via random walk MCMC. In total, we simulated 104 970 tsunamis originating from the Walanae/Selayar fault and 127 690 originating from the Flores thrust. This cost an estimated 110 yr of total compute time spread over 24 cores at a time and 20 chains, for nearly 2.5 months of real time computational cost.

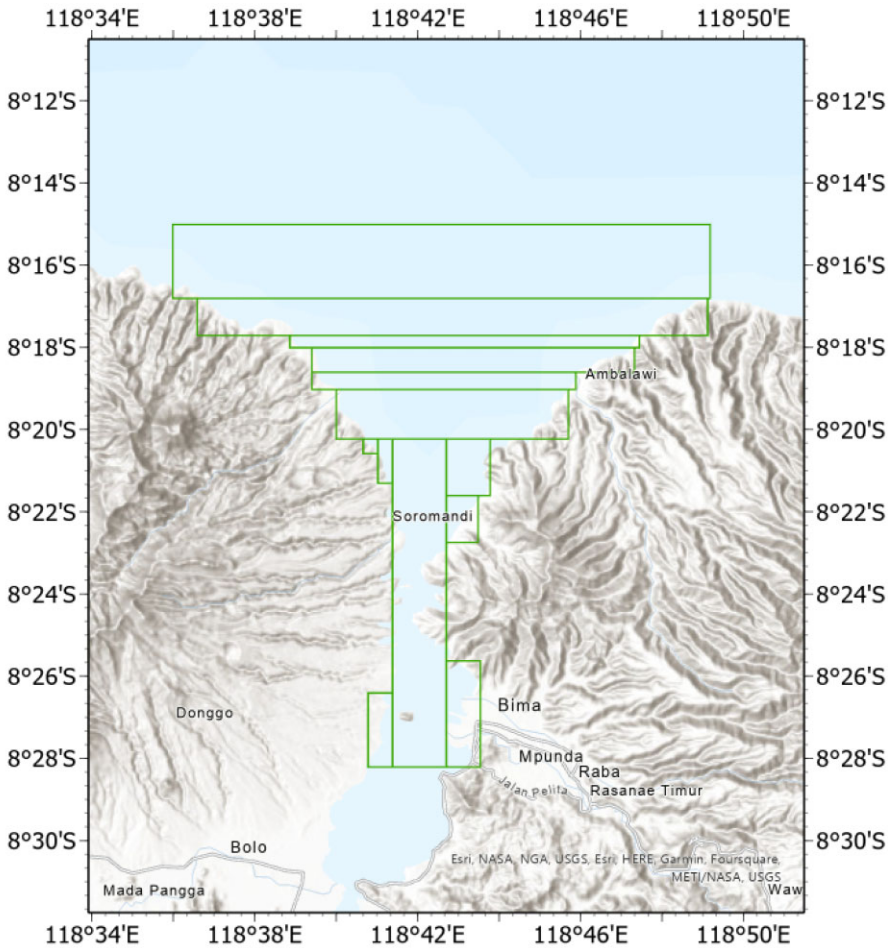

Figure 4. The rectangular regions where the resolution is fixed at the highest grid level near the port of Bima. We specified several subregions (shown as the green rectangles) that depict the regions of interest. Similar highly resolved regions are defined for all of the other observation locations as well.

Table 6. Entries of the diagonal covariance matrix for the random walk MCMC.

Sample parameter	Flores covariance	Walanae/Selayar covariance
Latitude (°)	0.086	0.05
Longitude (°)	0.11	0.04
Magnitude (M_w)	0.075	0.045
$\Delta \log l$ and $\Delta \log w$	0.0132	0.012
Δd (km)	0.525	0.55
$\Delta\beta$ (°)	2.7	2.55
$\Delta\gamma$ (°)	3.7	3.55
$\Delta\alpha$ (°)	3.15	3.05

The random walk step was initiated according to a diagonal covariance matrix with entries corresponding to the values given in Table 6. This covariance matrix was adjusted slightly (covariance values for dip offset $\Delta\beta$ and rake offset $\Delta\gamma$ as well as the longitude for Flores only were increased partway through the sampling) with the goal of getting close to a 0.25 acceptance ratio for both sets of chains. The averaged acceptance ratio for each different set of chains is depicted in Fig. 5. Note that the acceptance ratio for the Walanae/Selayar chains is slightly below the desired value, but the acceptance ratio for the Flores chains is still quite high, indicating that the sampling may be more aggressive on the Flores thrust then the covariance matrix described above. Despite this high acceptance rate, all ten chains were mixing very nicely in all of the relevant variables.

To verify the interchain mixing and ensure that the approximated posterior distribution is adequately converged, we computed the Gelman–Rubin diagnostic (Gelman *et al.* 1992, 2014) for all of the parameters from the posterior distribution as shown in Fig. 6. Note that the Flores posterior mixes at a slightly faster rate (the Gelman–Rubin diagnostic drops below 1.1 at a lower number of total samples), but in either case the diagnostic clearly indicates sufficient mixing between chains to satisfy the necessary invariance properties to anticipate that the posterior distributions are converging.

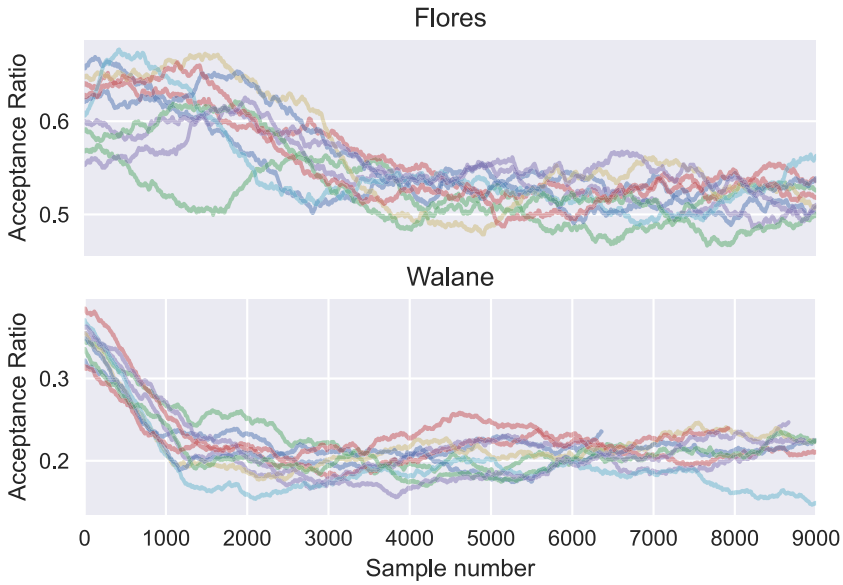

Figure 5. The acceptance ratio averaged over a 2000 sample interval for each fault's set of chains.

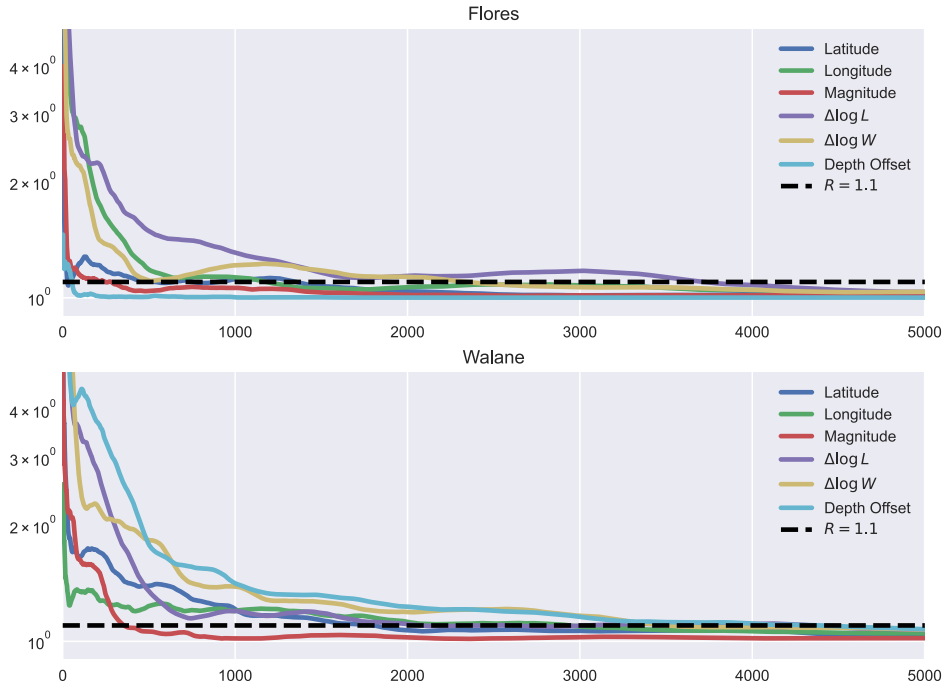

Figure 6. The Gelman–Rubin diagnostic displaying the relative interchain versus intrachain variance for each constructed posterior distribution. The dashed horizontal line is at the value of 1.1. As described in (Gelman *et al.* 1992, 2014) the diagnostic should drop below this line to indicate appropriate mixing of the sampled posterior. Note that this occurs for both posteriors before 5000 samples are collected (for every observable computed here) so we do not show the rest of the chain's data for samples beyond 5000.

4.2 Summary of posterior distribution

The primary description of the desired posterior distribution can be visualized via Figs 7 and 8. In particular, Fig. 7 displays a histogram of the sampled coordinate centroids for both faults with the left colourbar representing the density of samples on the Flores thrust and the right colourbar representing the density of samples on Walanae/Selayar. There are several items to note from this Figure alone. The coordinate centroid location along the Walanae/Selayar fault is in a very concentrated location near 120° longitude and −6.5° latitude. In contrast the sampling along the Flores thrust is far less focused, with preferred centroid coordinate locations spanning a wide range of longitudinal values, and a relatively wide range of latitudes near 119.5° to 120° longitude.

The prior distribution on coordinate centroid location for the Flores thrust did not force the earthquake coordinate centroid to be on the 'correct' side of the fault line (south of the blue curve in Fig. 7). This allowed for a surprising number of earthquake samples that were on the physically infeasible side of the fault (north of the blue curve), a region that appeared to actually be preferred to some

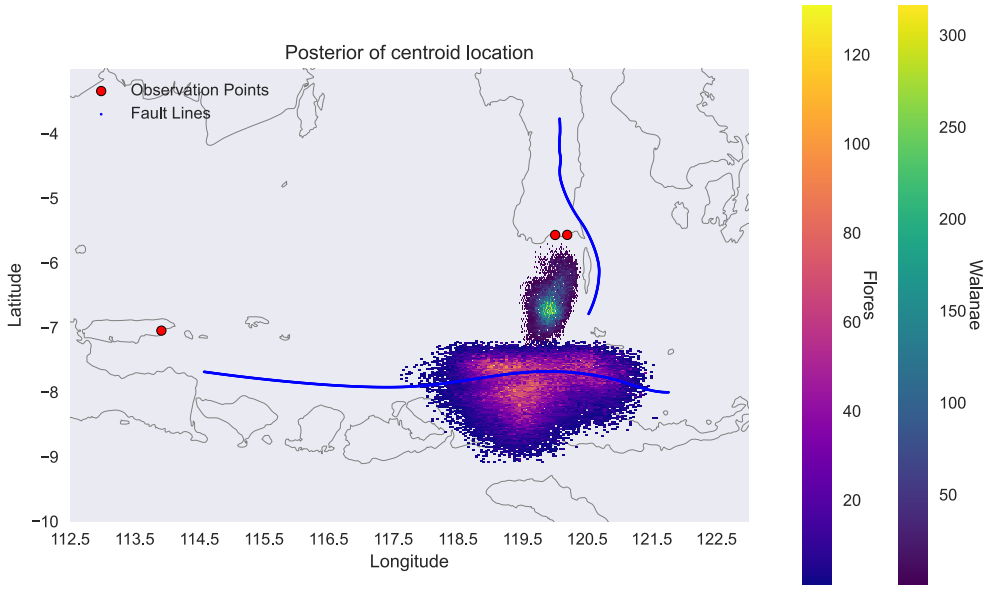

Figure 7. The relative posterior distribution (the actual units of the colourbars here are not comparable) of the earthquake centroid coordinates for both faults. Note that those earthquakes originating on the Walanae/Selayar fault will be oriented primarily north–south (in line with the fault line itself) whereas those earthquakes along the Flores thrust will be oriented primarily east–west. The prior distribution for the centroid coordinates of both of these faults is centred at 20 km deep on the interior of the fault, that is to the west of the Walanae/Selayar fault line (blue curve) and south of the Flores fault line.

extent by the sampling strategy employed here (there is a high concentration of coordinate centroids north of the blue curve in Fig. 7). This may indicate either that the Gaussian process prior is not sufficiently restrictive or (as discussed further below) the observational data prefers earthquakes centred north of the actual Flores fault. The coordinate centroids for the posterior on the Walanae/Selayar fault are on the 'correct' side of the fault, but they are further south than the prior prefers, indicating that observations are better matched with an earthquake coordinate centroid further south than the modelled Walanae/Selayar fault extends. In addition, the most preferred coordinate centroid locations for the Flores thrust (at least those that lie on the 'correct' side of the fault itself) line up with the curvature of the Walanae/Selayar fault. That is, the coordinate centroid locations from the two faults nearly line up in a north-south line as if the Walanae/Selayar fault extended all the way to the Flores thrust.

Fig. 8 depicts histograms of the sampled posterior distribution for all of the other sample parameters (omitting latitude and longitude which are depicted in Fig. 7). The offset parameters are depicted for both faults, and not Δd, $\Delta\alpha$, $\Delta\beta$ and $\Delta\gamma$ for the Flores fault. Fig. 9 displays the other earthquake parameters derived from the posterior distribution, that is the interesting Okada model parameters that are not already shown in Fig. 8. Finally, Fig. 10 depicts the histograms of the posterior predictive (output of each simulation for the observational data points) relative to the original observational probabilities.

5 DISCUSSION

5.1 Interpreting the posterior distribution

We first note that the prior and posterior distributions for all four offset parameters in Fig. 8 are nearly identical for the Walanae/Selayar fault. For this reason it is clear that the geometry of the Walanae/Selayar fault is not constrained by the data, that is the posterior simply recreates the prior distribution for these parameters. While a similar statement may be made regarding the strike offset for the Flores thrust, the other three offset parameters for Flores are significantly different from their prior distributions. It appears that depth, dip and rake are highly concentrated near the predicted mean values from the Gaussian process (the posterior distribution of the offset parameters is very narrowly centred around the origin) despite a wide prior distribution. This likely has less to do with the observational data itself, and more indicates that the Gaussian process provided a fairly robust fit to the fault in question.

On the other hand, there is a clear signal in both $\Delta\log l$ and $\Delta\log w$ for both faults that indicates that the observational data is a better match for smaller values of both of these parameters. Smaller values of these parameters for a fixed magnitude corresponds to a larger slip length than expected, that is this indicates that the earthquakes that best match the data have very large slip as seen in Fig. 9. We see that the most probable slip that matched the data for both faults was over 10 m with a definite preference for larger slip. The slip on the Walanae/Selayar posterior is slightly smaller, with a maximum probability estimate close to 8 m rather than 10 m, and a slightly less positive bias towards larger slip. This tendency towards an unexpectedly large slip was noted in Ringer *et al.* (2021) for the 1852 Banda Sea earthquake in Eastern Indonesia where the Bayesian technique used here was first introduced, and is likely a by-product of using a uniform homogeneous slip distribution (Geist 2002; Davies 2019; Melgar *et al.* 2019; Davies & Griffin 2020). Future studies will consider the potential discretization effects and selection of hyperparameters including the potential non-uniformity of the slip distribution in the forward model that could lead to a preference for smaller rectangular area, large slip ruptures.

Note from Fig. 9 that a hypothesized Flores earthquake is less constrained in size as the length and width have a significantly wider histogram that extends to much larger values than earthquakes hypothesized for the Walanae/Selayar fault. This is likely because, as discussed in more detail below, the Flores posterior tends to favour high magnitude earthquakes. It is also interesting to note that in

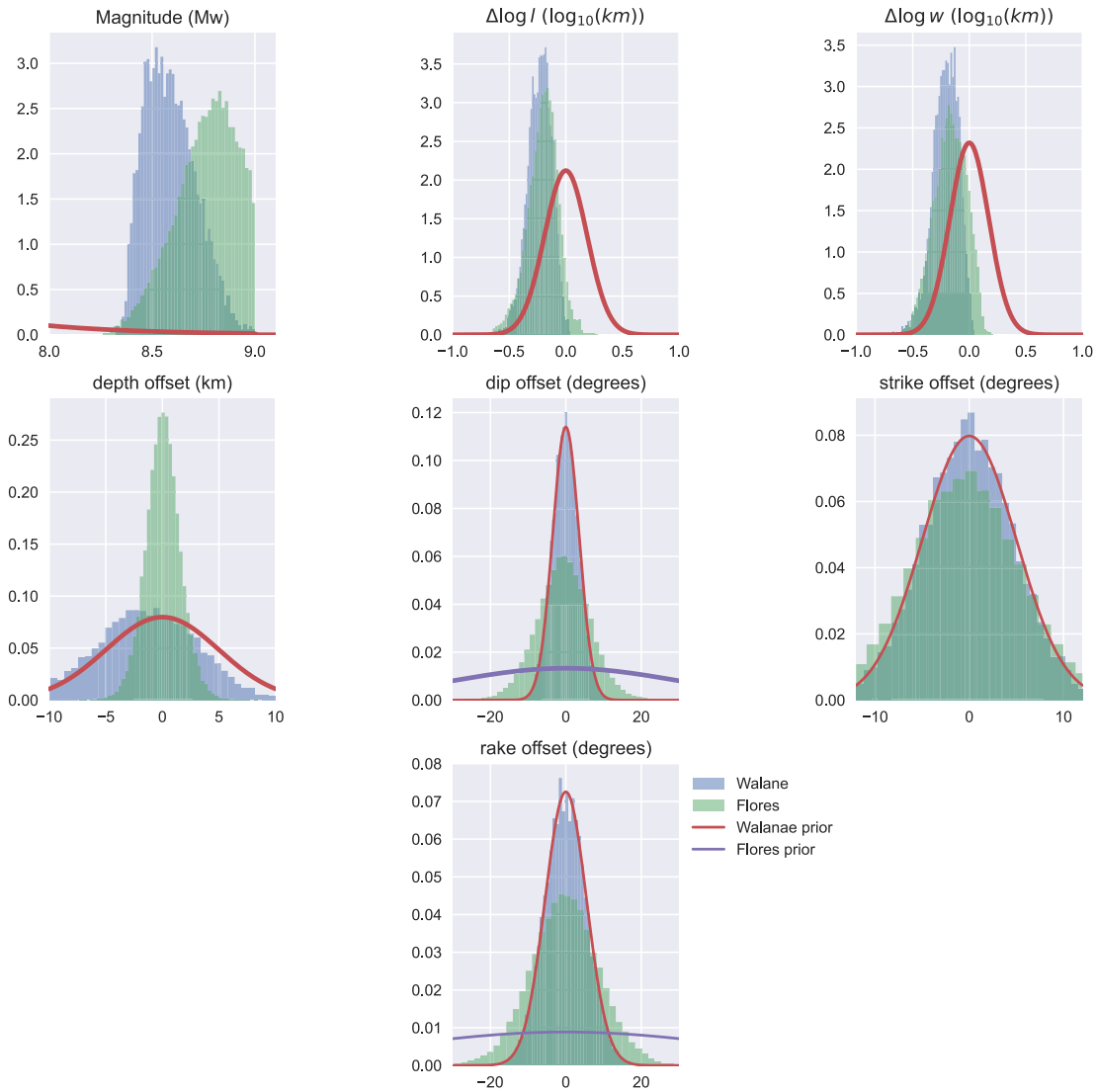

Figure 8. The posterior samples for all of the relevant sample parameters from both faults compared against the prior distributions. When the prior distribution for both faults is identical, it is depicted as the single red curve. The histograms here display the offset parameters for both faults as well as the magnitude. Note that the vertical labels on these plots are set by the arbitrary normalization factor used to visualize the prior distributions, that is the reader should not read anything into the relative differences between the vertical labels. The units for each variable are indicated in the title of each plot.

contrast to the magnitude derived parameters, the depth of the Flores posterior is more constrained than the depth for Walanae/Selayar. This is likely a result of a more data-driven prior distribution on the Flores fault (the Gaussian process does a better job at modelling the fault than the planar regression model) whereas the Walanae/Selayar prior is a nearly linear fit and hence the depth values of the modelled fault are highly suspect.

As previously described, the prior distribution on magnitude was the exponential Richter distribution that exponentially decays with growing magnitude as indicated by the red curve in the upper left plot of Fig. 8. Due to the size of the Flores and Walanae/Selayar faults, we also truncated the magnitude at 9.0 M_w (although this restriction will be removed from future studies in addition to the inclusion of heterogeneous slip distributions) to ensure physically reasonable earthquakes were observed. As shown, the observational accounts best matched with earthquakes of high magnitude, particularly for originating earthquakes along the Flores thrust. The earthquakes sampled from the Walanae/Selayar posterior were also quite large for the size of the Walanae/Selayar fault with the most likely value near 8.5 M_w.

The high magnitude preference for both posterior distributions is in line with the observation made previously that the slip was quite large for both of these earthquakes. It is likely that neither the Walanae/Selayar fault nor the Flores thrust are large enough to sustain an 8.5 M_w earthquake with the expected relationship maintained between length, width and slip. The apparent over-estimation on magnitude is likely a result of the uniform slip distribution assumed throughout this study. Despite this restriction on the model, the observational data indicates that large magnitude events are necessary for the tsunami observations to match the historical record. The apparent trade off here is satisfied with large (but not extreme) magnitude earthquakes that are shorter and narrower, but with very high, uniform slip length. An alternative hypothesis is that the earthquake was triggered on both the Walanae/Selayar and Flores faults, perhaps allowing for a smaller magnitude event on both nearly simultaneously.

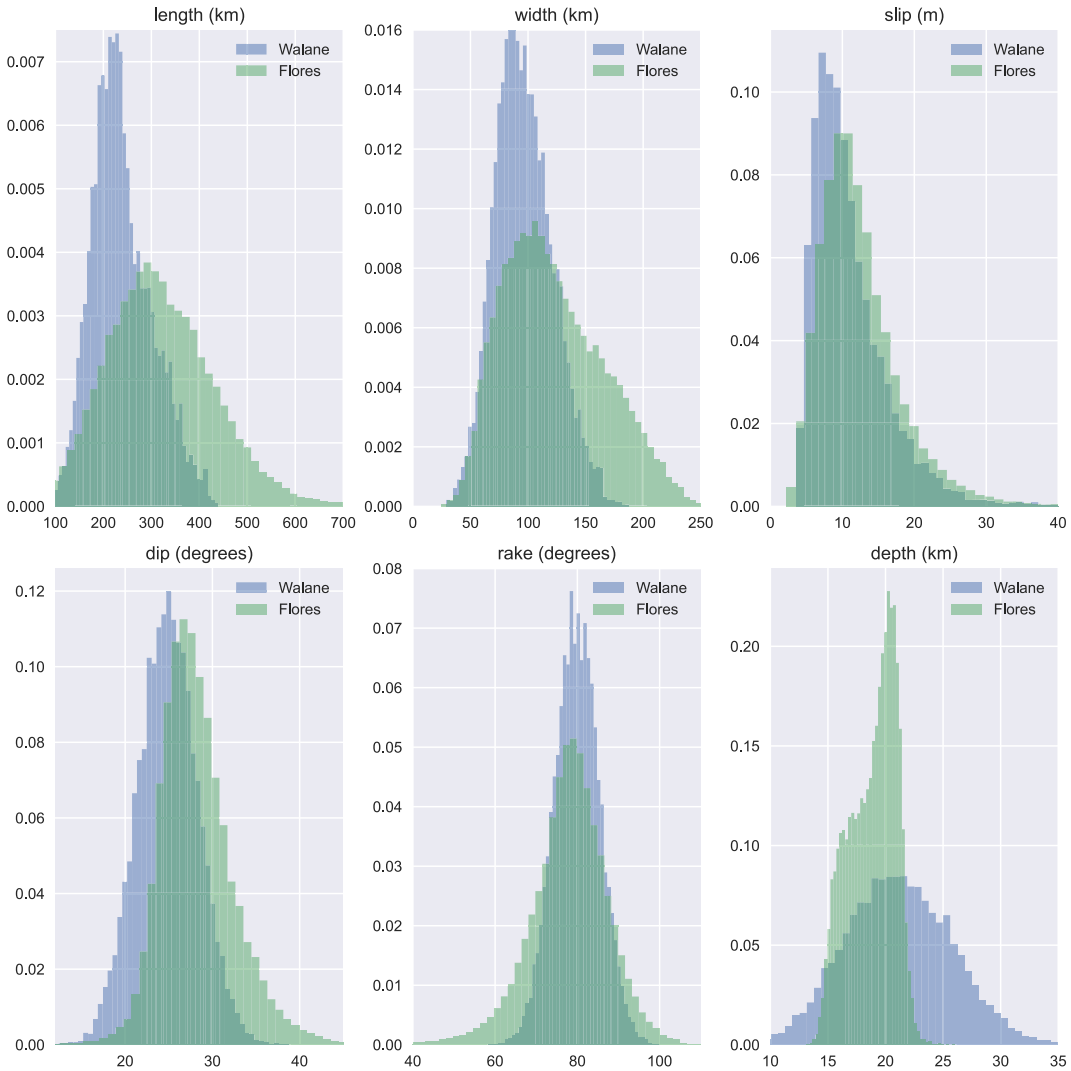

Figure 9. Histograms of the posterior distribution on the actual earthquake parameters (rather than sample parameters) for each fault. The strike is omitted as it is fundamentally different for each fault (Walanae/Selayar runs north–south while Flores runs primarily east–west), and a comparison between the strike for the two posterior distributions is not informative.

5.2 The impact of the posterior predictive

Finally, we comment on some observations that arise from the posterior predictive (Fig. 10). The extreme wave height from the observation in Bulukumba is clearly not achieved for either posterior distribution, leading us to believe that either the historical observation which claimed a wave height of 60–80 feet (18–24 m) was overexaggerated, or some other non-linear, local effects were at play. In particular, it is possible that a submarine landslide caused by the earthquake could generate a wave of this magnitude at least locally. This hypothesis is reasonable when we consider that the wave heights at Nipa-Nipa generated from either fault are near the observational probabilities, noting that Nipa-Nipa is geographically very close to Bulukumba so that it is highly unlikely that Bulukumba would have a wave near 20 m whereas Nipa-Nipa only sustained one of 4–5 m.

The arrival time in Bulukumba has a few peculiarities. The large number of arrival times at time 0 for the Walanae/Selayar posterior arise because a significant number of the Walanae/Selayar earthquakes have a rupture zone overlapping the observation locations at Bulukumba so that the sea surface is uplifted after a single time step of the integration time. This introduces a slight numerical change in sea surface height that triggers the cut-off we established indicating the arrival of the wave. Beside these events, it is apparent that the posterior predictive from the Walanae/Selayar fault matches the observational distribution quite well for the Bulukumba arrival time whereas the Flores posterior indicates a much longer arrival time to Bulukumba than anticipated. This should be taken with a grain of salt however as the observational probability distribution for the wave's arrival at Bulukumba is quite uncertain itself.

The observational distribution for wave height at Sumenep appears to better match the Flores posterior predictive except that for this particular observation we recall that the only statement was that the wave was observed at Sumenep, that is the observational distribution at this location is not very precise.

The arrival time at Sumenep clearly does not agree well with either posterior predictive, but it is also certain that the Walanae/Selayar posterior is a much better fit than the Flores as waves originating from the Walanae/Selayar fault take over 3 hr to arrive at Sumenep while most tsunamis originating from Flores arrive just under 3 hr. This particular comparison should not be weighted too heavily though, as neither fault generates a tsunami

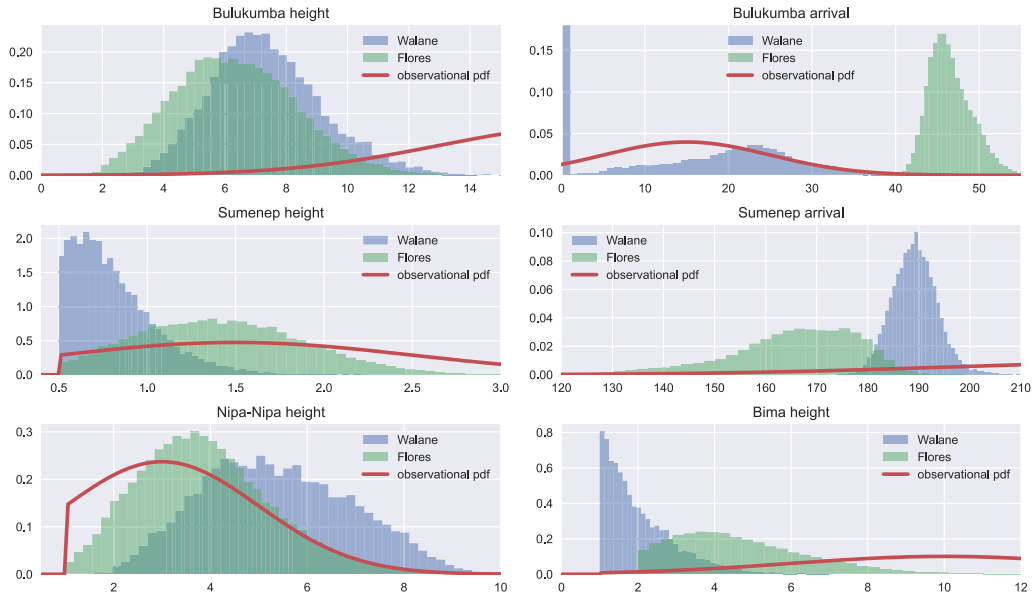

Figure 10. Posterior samples from both hypothesized faults plotted against the observational probabilities assigned to each observation.

whose initial wave arrives in 4 hr which is the observational value assuming that Eastern Java and Sulawesi relied on a time that was approximately one hour off from each other. A partial explanation for this is that the initial wave is not the one recorded in the historical record, but that a secondary wave is the one observed in Sumenep. We did not collect the arrival times for the secondary waves for all 200 000+ simulated earthquakes, but from repeat simulation of a few events we did note that some of the later waves from both the Walanae/Selayar and Flores faults were larger than the initial wave with corresponding arrival times exceeding 210 min (for Flores) and 240 min (for Walanae/Selayar). Low resolution bathymetry may also play a role in faster predicted versus actual arrival times.

The posterior predictive wave height at Bima is also not a great match with the observational data for either fault, although earthquakes generated from the Flores thrust match the observation better. In essence the generated earthquakes are underestimating the wave height in Bima. There are several potential reasons for this, one of which may simply be that the bathymetric resolution is not sufficient to capture the amplification of the wave entering the bay. Even with the type of amplification that may occur, the Walanae/Selayar posterior clearly underestimates the wave height at Bima as it is hard to imagine a 2 m wave having sufficient buoyancy and force to 'fling' ships far inland.

6 CONCLUSIONS

The Bayesian approach toward identifying characteristics of earthquakes using anecdotal historical accounts of tsunamis first introduced in (Ringer *et al.* 2021) has been applied to the 1820 south Sulawesi earthquake and consequent tsunami. Using the Bayesian framework, we have simulated over to 200 000 different events, searching through parameter space for earthquakes that probabilistically best match the interpreted historical record. Hypothesizing that the earthquake originated purely from either the Flores or Walanae/Selayar faults does not yield a posterior distribution that appears to match the data perfectly, although we have strong statistical reasoning to assert that the Walanae/Selayar fault was far more likely to be the source than the Flores thrust.

To further investigate this event and hopefully ascertain the source of the recorded tsunami, we postulate these additional potential hypotheses: (1) A landslide near where the Walanae/Selayar Fault goes offshore (likely very near Bulukumba itself) that can produce the significant wave heights recorded near the Fort. (2) The dual rupture of both the Walanae/Selayar and Flores faults. Although a time-dependent rupture is clearly more physically relevant, we will restrict our attention to an instantaneous rupture of both faults simultaneously, as it is unlikely that our limited observations of tsunami impacts will provide enough detail to constrain a more sophisticated rupture model. (3) Non-uniform slip distributions have been shown to directly effect the tsunami wave height. We will determine a parametrization of the Okada model that allows for this additional feature, and is conducive to our Bayesian approach.

Further extensions of this Bayesian approach to historical tsunamis will be carried out both to improve the sampling procedure, and to investigate other events with the goal of providing a thorough description of past seismicity in the Indonesian region.

ACKNOWLEDGMENTS

Beyond the authors listed on this paper, there are several students who have come through BYU that have contributed to the formation of these results. These include but are not limited to: H. Ringer, S. Giddens, M. Morrise, C. Noorda, J. Callahan, K. Lightheart, C. Kesler and C. Herrera. In particular, we wish to thank N. Thompson for his assistance with improving the presentation of some of the figures reported here. We also would like to thank N. Glatt-Holtz for inspiring this work several years ago, and useful conversations with R. LeVeque, V. Martinez, C. Mondaini, A. Holbrook, as well as a host of other colleagues who have provided useful feedback and guidance over the years.

We also acknowledge generous financial support from the BYU Mathematics and Geology Departments, the College of Physical and Mathematical Sciences, as well as Geoscientists Without Borders. JPW was partially supported by NSF grant DMS-2206762, and JAK was partially supported by NSF grant DMS-2108791.

The authors are also indebted to two anonymous reviewers whose comments greatly improved this paper and made its readability vastly improved.

DATA AVAILABILITY

All of the relevant code that generated the data provided in this paper appears in Whitehead (2023). The data itself can be viewed via the graphical interface provided at http://tsunami.byu.edu/whitehead-lab.

SUPPORTING INFORMATION

Supplementary data are available at *GJI* online.

suppl_data

Please note: Oxford University Press is not responsible for the content or functionality of any supporting materials supplied by the authors. Any queries (other than missing material) should be directed to the corresponding author for the paper.

REFERENCES

Abrahamson, N., Gregor, N. & Addo, K., 2016. BC Hydro ground motion prediction equations for subduction earthquakes, *Earthq. Spectra,* **32**(1), 23–44.

An, C., Liu, H., Ren, Z. & Yuan, Y., 2018. Prediction of tsunami waves by uniform slip models, *J. geophys. Res.,* **123**(11), 8366–8382.

Anonymous, 1821. *Bataviasche Courant*.

Anonymous, 1852. Van batavia naar timor koepang, *Tijdschrift voor Neerlandsch Indië,* **14**(1), 1–22.

Barkan, R. & Ten Brink, U., 2010. Tsunami simulations of the 1867 Virgin Island earthquake: constraints on epicenter location and fault parameters, *Bull. seism. Soc. Am.,* **100**(3), 995–1009.

Berger, M.J., George, D.L., LeVeque, R.J. & Mandli, K.T., 2011. The GeoClaw software for depth-averaged flows with adaptive refinement, *Adv. Water Resour.,* **34**(9), 1195–1206.

Blaser, L., Krüger, F., Ohrnberger, M. & Scherbaum, F., 2010. Scaling relations of earthquake source parameter estimates with special focus on subduction environment, *Bull. seism. Soc. Am.,* **100**(6), 2914–2926.

Bondevik, S., 2008. Earth science: the sands of tsunami time, *Nature,* **455**(7217), 1183–1184 .

Bryant, E., Walsh, G. & Abbott, D., 2007. Cosmogenic mega-tsunami in the Australia region: are they supported by Aboriginal and Maori legends?, *Geol. Soc., Lond., Spec. Publ.,* **273**(1), 203–214.

Butler, R., Walsh, D. & Richards, K., 2017. Extreme tsunami inundation in Hawai'i from Aleutian–Alaska subduction zone earthquakes, *Nat. Haz.,* **85**(3), 1591–1619.

Cipta, A., Robiana, R., Griffin, J., Horspool, N., Hidayati, S. & Cummins, P.R., 2017. A probabilistic seismic hazard assessment for Sulawesi, Indonesia, *Geol. Soc., Lond., Spec. Publ.,* **441**(1), 133–152.

Davies, G., 2019. Tsunami variability from uncalibrated stochastic earthquake models: tests against deep ocean observations 2006–2016, *Geophys. J. Int.,* **218**(3), 1939–1960.

Davies, G. & Griffin, J., 2020. Sensitivity of probabilistic tsunami hazard assessment to far-field earthquake slip complexity and rigidity depth-dependence: case study of Australia, *Pure appl. Geophys.,* **177,** 1521–1548.

Davis, B. & LeVeque, R., 2016. Adjoint methods for guiding adaptive mesh refinement in tsunami modeling, *Pure appl. Geophys.,* **173**(12), 4055–4074.

Fisher, T.L. & Harris, R.A., 2016. Reconstruction of 1852 Banda Arc megathrust earthquake and tsunami, *Nat. Haz.,* **83**(1), 667–689.

Geist, E.L., 2002. Complex earthquake rupture and local tsunamis, *J. geophys. Res.,* **107**(B5), ESE 2–1-ESE 2-15.

Gelman, A., Rubin, D.B. *et al.*, 1992. Inference from iterative simulation using multiple sequences, *Stat. Sci.,* **7**(4), 457–472.

Gelman, A., Gilks, W.R. & Roberts, G.O., 1997. Weak convergence and optimal scaling of random walk Metropolis algorithms, *Ann. Appl. Prob.,* **7**(1), 110–120.

Gelman, A., Carlin, J.B., Stern, H.S. & Rubin, D.B., 2014. *Bayesian Data Analysis,* Vol. **2,** Taylor & Francis.

González, F.I., LeVeque, R.J., Chamberlain, P., Hirai, B., Varkovitzky, J. & George, D.L., 2011. Validation of the GeoClaw model, in *NTHMP MMS Tsunami Inundation Model Validation Workshop,* GeoClaw Tsunami Modeling Group.

Griffin, J., Nguyen, N., Cummins, P. & Cipta, A., 2018. Historical earthquakes of the Eastern Sunda Arc: source mechanisms and intensity-based testing of Indonesia's National Seismic Hazard Assessment, *Bull. seism. Soc. Am.,* **109**(1), 43–65.

Grimes, B.D., 2006. Mapping Buru: the politics of territory and settlement on an Eastern Indonesian Island, in *Sharing the Earth, Dividing the Land: Land and Territory in the Austronesian World,* pp. 135–155, ed. Reuter, T., ANU Press.

Hamilton, W.B., 1979. *Tectonics of the Indonesian Region,* Vol. **1078,** US Government Printing Office.

Harris, R., 2011. The nature of the Banda Arc–continent collision in the Timor region, in *Arc-Continent Collision,* pp. 163–211, Springer.

Harris, R. & Major, J., 2016. Waves of destruction in the East Indies: the Wichmann catalogue of earthquakes and tsunami in the Indonesian region from 1538 to 1877, *Geol. Soc., Lond., Spec. Publ.,* **441**(1), doi:10.1144/SP441.2.

Jankaew, K., Atwater, B.F., Sawai, Y., Choowong, M., Charoentitirat, T., Martin, M.E. & Prendergast, A., 2008. Medieval forewarning of the 2004 Indian Ocean tsunami in Thailand, *Nature,* **455**(7217), 1228–1231.

Jaya, A., Nishikawa, O. & Jumadil, S., 2020. Paleoseismic of the Walanae Fault Zone in the South Arm of Sulawesi, Indonesia, Tech. rep., EasyChair.

Kaipio, J. & Somersalo, E., 2005. *Statistical and Computational Inverse Problems,* Vol. 160 of Applied Mathematical Sciences, Springer Science & Business Media.

Krometis, J.A., Ringer, H., Whitehead, J.P., Glatt-Holtz, N.E. & Harris, R.A., 2021. *Embracing uncertainty in" small data" problems: Estimating earthquakes from historical anecdotes,* preprint (arXiv:2106.07797).

Lay, T., 2018. A review of the rupture characteristics of the 2011 Tohoku-Oki Mw 9.1 earthquake, *Tectonophysics,* **733,** 4–36.

LeVeque, R.J., George, D.L. & Berger, M.J., 2011. Tsunami modelling with adaptively refined finite volume methods, *Acta Numer.,* **20,** 211–289.

Liu, Z. Y.C. & Harris, R.A., 2014. Discovery of possible mega-thrust earthquake along the Seram Trough from records of 1629 tsunami in eastern Indonesian region, *Nat. Haz.,* **72,** 1311–1328.

Martin, S.S., Li, L., Okal, E.A., Morin, J., Tetteroo, A. E.G., Switzer, A.D. & Sieh, K.E., 2019. Reassessment of the 1907 Sumatra "Tsunami Earthquake" based on macroseismic, seismological, and tsunami observations, and modeling, *Pure appl. Geophys.,* **176,** 2831–2868.

Martin, S.S., Cummins, P.R. & Meltzner, A.J., 2022. Gempa Nusantara: a database of 7380 macroseismic observations for 1200 historical earthquakes in Indonesia from 1546 to 1950, *Bull. seism. Soc. Am.,* **112**(6), 2958–2980.

Melgar, D., Williamson, A.L. & Salazar-Monroy, E.F., 2019. Differences between heterogenous and homogenous slip in regional tsunami hazards modelling, *Geophys. J. Int.,* **219**(1), 553–562.

Meltzner, A.J. *et al.*, 2010. Coral evidence for earthquake recurrence and an AD 1390–1455 cluster at the south end of the 2004 Aceh–Andaman rupture, *J. geophys. Res.,* **115**(B10), doi:10.1029/2010JB007499.

Meltzner, A.J., Sieh, K., Chiang, H.-W., Shen, C.-C., Suwargadi, B.W., Natawidjaja, D.H., Philibosian, B. & Briggs, R.W., 2012. Persistent termini of 2004- and 2005-like ruptures of the Sunda megathrust, *J. geophys. Res.,* **117**(B4), doi:10.1029/2011JB008888.

Meltzner, A.J. *et al.*, 2015. Time-varying interseismic strain rates and similar seismic ruptures on the Nias–Simeulue patch of the Sunda megathrust, *Quater. Sci. Rev.,* **122,** 258–281.

Monecke, K., Finger, W., Klarer, D., Kongko, W., McAdoo, B.G., Moore, A.L. & Sudrajat, S.U., 2008. A 1,000-year sediment record of tsunami recurrence in northern Sumatra, *Nature,* **455**(7217), 1232–1234.

Nanayama, F., Satake, K., Furukawa, R., Shimokawa, K., Atwater, B.F., Shigeno, K. & Yamaki, S., 2003. Unusually large earthquakes inferred from tsunami deposits along the Kuril trench, *Nature,* **424**(6949), 660–663.

Newcomb, K. & McCann, W., 1987. Seismic history and seismotectonics of the Sunda Arc, *J. geophys. Res.,* **92**(B1), 421–439.

Nguyen, N., Cipta, A., Cummins, P. & Griffin, J., 2015. *Indonesia's Historical Earthquakes: Modelled Examples for Improving the National Hazard Map,* Geoscience Australia.

Nugroho, H., Harris, R., Lestariya, A.W. & Maruf, B., 2009. Plate boundary reorganization in the active Banda Arc–continent collision: Insights from new GPS measurements, *Tectonophysics,* **479**(1–2), 52–65.

Okada, Y., 1985. Surface deformation due to shear and tensile faults in a half-space, *Bull. seism. Soc. Am.,* **75**(4), 1135–1154.

Okada, Y., 1992. Internal deformation due to shear and tensile faults in a half-space, *Bull. seism. Soc. Am.,* **82**(2), 1018–1040.

Rawlinson, N., Fichtner, A., Sambridge, M. & Young, M.K., 2014. Seismic tomography and the assessment of uncertainty, *Adv. Geophys.,* **55,** 1–76.

Reid, A., 2016. Two hitherto unknown Indonesian tsunamis of the seventeenth century: probabilities and context, *J. SE Asian Stud.,* **47**(1), 88–108.

Reinwardt, C. G.C., 1858. *Reis naar het oostelijk gedeelte van den Indischen Archipel in het jaar 1821. Uit zijne nagelaten aanteekeningen opgestelt met een levensberigt en bijlagen vermeerderd door WH de Vriese,* Muller.

Ringer, H. *et al.*, 2021. Methodological reconstruction of historical seismic events from anecdotal accounts of destructive tsunamis: a case study for the great 1852 Banda arc mega-thrust earthquake and tsunami, *J. geophys. Res.,* **126**(4), e2020JB021107.

Sarsito, D.A., Susilo, S., Rudyawan, A., Muhammad, N.A., Andreas, H. & Pradipta, D., 2019. Walanae fault kinematic deduced from geometric geodetic GNSS GPS monitoring, in *Proceedings of the E3S Web of Conference, International Symposium on Global Navigation Satellite System 2018 (ISGNSS 2018),* Vol. **94,** EDP Sciences.

Sieh, K. *et al.*, 2008. Earthquake supercycles inferred from sea-level changes recorded in the corals of west Sumatra, *Science,* **322**(5908), 1674–1678.

Silver, E.A., Reed, D., McCaffrey, R. & Joyodiwiryo, Y., 1983. Back arc thrusting in the eastern Sunda arc, Indonesia: a consequence of arc-continent collision, *J. geophys. Res.,* **88**(B9), 7429–7448.

Simons, W. *et al.*, 2007. A decade of GPS in Southeast Asia: resolving Sundaland motion and boundaries, *J. geophys. Res.,* **112**(B6), doi:10.1029/2005JB003868.

Tanioka, Y. & Sataka, K., 1996. Fault parameters of the 1896 Sanriku tsunami earthquake estimated from tsunami numerical modeling, *Geophys. Res. Lett.,* **23**(13), 1549–1552.

Van Eysinga, S.R., 1831. *Verschillende reizen en lotgevallen van S. Roorda van Eysinga: uitgegeven door deszelfs zoon PP Roorda van Eijsinga,* Vol. **2,** Johannes van der Hey en zoon.

Wells, D.L. & Coppersmith, K.J., 1994. New empirical relationships among magnitude, rupture length, rupture width, rupture area, and surface displacement, *Bull. seism. Soc. Am.,* **84**(4), 974–1002.

Whitehead, J.P., 2023. *tsunamibayes: 1820 South Sulawesi tsunami,* doi:10.5281/zenodo.4068546.

Wichmann, A., 1918. The earthquakes of the Indian archipelago to 1857, *Verhandl. Koninkl. Akad. van Wetenschappen, 2nd sec,* **20**(4), 1–193.

Wichmann, A., 1922. The earthquakes of the Indian archipelago from 1858 to 1877, *Verhandl. Koninkl. Akad. van Wetenschappen, 2nd sec,* **22**(5), 1–209.

Williams, C.K. & Rasmussen, C.E., 2006. *Gaussian Processes for Machine Learning,* Vol. **2,** MIT Press.